Journal Name

ARTICLE

Redox-Mediated Dissolution of Paramagnetic Nanolids to Achieve Smart Theranostic System

Aifei Wang,[a] Mingyi Guo,[a,e] Nan Wang,[c] Jianyun Zhao,[d] Wenxiu Qi,[d] Faheem Muhammad,[d] Liang Chen,[c] Yingjie Guo,[d] Nam-Trung Nguyen[b] and Guangshan Zhu*[a,b]

Manganese oxide (Mn_3O_4) nanoparticles have recently emerged as promising T1 contrast agent. In this study, for the first time, we demonstrated an interaction of Mn_3O_4 with biological system, and found a redox sensitive behavior of these paramagnetic nanoparticles in intracellular reducing environment. Inspired by these findings, we for the first time used this interaction for some therapeutic advantages and designed a versatile mesoporous silica based nanotheranostic system to realize redox-activated enhanced magnetic resonance imaging and responsive anticancer drug delivery. Contrary to previous reports, we firstly prepared high quality amine terminated hydrophilic Mn_3O_4 nanolids, without using multistep ligand exchange strategies. The resulting water stable and small-sized Mn_3O_4 nanolids were subsequently used as nanolids to cap drug loaded nanochannels of porous carrier. Exposure to highly prevalent intracellular reducing environment resulted in the steady-state dissolution of these nanolids and attained an intelligent drug release. Furthermore, the redox receptive dissolution of paramagnetic Mn_3O_4 nanolids into Mn^{2+} in turn increases the T1 signal to twofold, providing an added opportunity to even track the feedback of therapy. This study, in addition to simultaneously realizing drug delivery and imaging, also provides a new insight into the fate and interaction of manganese oxide nanoparticles with components of biological systems.

1. Introduction

Nanoparticle based therapeutics obviously has an intrinsic potential to bring a major shift in the landscape of the pharmaceutical industry.[1-3] Evidently, scores of nanobased medicine have been approved by the US Food and Drug Administration (FDA) for clinical use, and many more are in clinical or preclinical pipelines.[4, 5] Liposomes,[6] polymers,[7] dendrimers,[8] carbon nanotubes,[9] gold[10] and magnetic nanoparticle11 based therapeutics are few of the widely explored nanocarriers to increase the efficacy of various anticancer drugs due to enhanced permeability and retention (EPR) effect of cancer tissues. Furthermore, different pathophysiological conditions and ligand carrying capabilities of nanocarriers also ensured target specific intratumoral drug accumulation. Among these libraries of sophisticated nanocarriers, mesoporous silica nanoparticles (MSN) have recently emerged as a promising nanoplatform to engineer a wide array of therapeutic and diagnostic nanoconstructs.[12, 13]

In particular, considering the stimuli responsive drug delivery, mesoporous silica has proved its niche in this realm, due to the presence of well-defined nanochannels and outer surface which can be manipulated to accommodate different environmental conditions. Using this concept of gate keeping, several research groups have attempted to design different stimuli responsive nanosystem to inhibit the premature release of cytotoxic drugs. To manipulate diverse kinds of capping entities, both external and internal triggers such as pH,[14-16] redox,[17-20] light,[21, 22] enzymes,[23] magnetic,[24] electric field and competitive binding,[25] have been employed to regulate the release of cytotoxic molecules according to environmental requirements. In this respect, our group has recently reported a pH responsive nanovehicle by use of the acid sensitive nature of ZnO quantum dots to release an anticancer drug from mesopores.[26]

Besides stimuli responsive drug delivery, there has also been an overwhelming research interest in the development of theranostic nanomaterials for simultaneous imaging and therapy. In view of that, diverse kinds of biological imaging agents have been incorporated into mesoporous silica, to realize X-ray computed tomography (CT)[27], fluorescence,[28] near IR (NIR)29, and magnetic resonance imaging (MRI).[30-32] Currently, MRI is one of the most dominant in vivo imaging technologies; however clinically, to improve the quality of

image, contrast enhancement agents are used to increase the signal difference between the area of concern and the background. In the last few years, Hyeon's research group reported several studies that incorporated MRI agents into mesoporous silica.[33-35] Recently, they have fabricated a core shell MnO@MSN nanostructure for labelling stem cells.[35] Very recently, manganese oxides based nanoparticles has been developed as T1 contrast agents for MRI signal enhancement.[36, 37]

Despite this phenomenal research activity in nanotheranostics, more specific and precise manipulation are needed to not only achieve stimuli responsive drug release, but also improve the quality of imaging for better diagnosis or subsequent feedback of chemotherapy. Till now, numerous redox responsive systems have been developed for intracellular release of several therapeutic entities, by using widely known reducing agents such as dithiothreitol (DTT), mercaptoethanol and glutathione (GSH).[17, 18] Mechanistically, the cleavage of disulphide bond has been a sole option in all previously reported redox responsive system to uncap the nanochannels.

Through a paramagnetic nanolid dissolution strategy, instead of disulphide bond cleavage, herein we developed an intelligent dual-purpose nanocarrier to achieve both simultaneous therapy and MRI. The paramagnetic nanocrystals (Mn_3O_4) have been demonstrated to disintegrate in response to intracellular redox trigger GSH. Exposure of drug loaded Mn_3O_4@MSN nanoformulation to glutathione resulted in the dissolution of Mn_3O_4 nanolids, thus releasing the drug molecules from MSN (functioning mechanism is illustrated in Fig. 1). Moreover, mesoporous surface tethered redox-sensitive Mn_3O_4 nanocrystals simultaneously served as nanolids and provided an opportunity for enhanced MR images due to the presence of free Mn(II) ions released after the dissolution of nanolids.
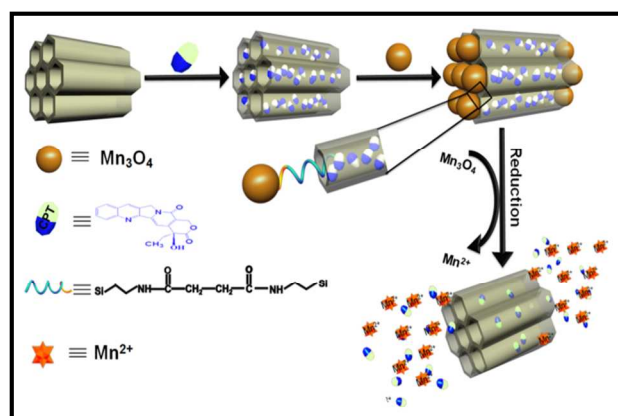
Fig. 1 Schematic illustration of the synthesis of Mn_3O_4 paramagnetic nanocrystals capped MSN and intracellular redox trigger release of the anticancer Drug (camptothecin) from MSN.

2. Experimental

2.1. Materials and instrumentation

Cetyltrimethylammonium bromide (CTAB), tetraethylorthosilicate (TEOS), 3-Aminopropyltriethoxysilane (APTES), 1-(3-(dimethylamino)propyl)-3-ethylcarbodiimide hydrochloride (EDC·HCl), Camptothecin (CPT), Glutathione (GSH) and Dithiothreitol (DTT) were purchased from Aladdin Reagent Company. 3-[4,5-dimethylthialzol-2-yl]-2,5-diphenyltetrazolium bromide (MTT) was purchased from Sigma-Aldrich. The morphologies and detailed structure of the samples were recorded using JEOL JSM-6700F field-emission scanning electron microscope (SEM) and FEI Tecnai G2 F20 S-TWIN transmission electron microscope (TEM). The powder XRD patterns were recorded on a Rigaku D/Ma 2550 X-ray diffractometer with Cu-Kα radiation (λ = 1.5418 Å). Fourier transform infrared (FTIR) spectra were collected on a Nicolet Impact 410 FTIR spectrometer in the range of 400 - 4000 cm−1. Elemental analysis was carried out on Perkin-Elmer ICP-OES Optima 3300DV. X-ray photoelectron spectroscopy (XPS) was performed using an ESCALAB 250 spectrometer. Raman spectra were obtained with a Renishaw Raman system model 1000 spectrometer.

2.2. Synthesis of water dispersible Mn_3O_4 nanocrystals

Mn_3O_4 nanocrystals were synthesized by a facile hydrothermal method, using $Mn(CH_3COOH)_2·4H_2O$ as manganese source. First of all, $Mn(CH_3COOH)_2·4H_2O$ (10 mmol) was dissolved in 70 mL N,N-dimethylformamide (DMF). Then, the transparent solution was transferred into Teflon-lined autoclave and heated at 160 °C for 8 h, cooled down to room temperature naturally. After the synthesis of Mn_3O_4 nanocrystal, they were rendered water soluble by functionalization with amine moiety. The as-synthesized transparent solution of Mn_3O_4 was transferred into a round bottom flask and temperature was raised to 130 °C, followed by the addition of 500 μL of APTES. The resulting brownish precipitate was afterwards centrifuged and washed with ethanol, dried in air.

2.3. Synthesis and modification of MSN

MSN was prepared as described previously. 0.5 g of CTAB was first dissolved in 240 mL deionized water. Sodium hydroxide aqueous solution (2M, 1.8 mL) was added to the CTAB solution, and then the reaction temperature was raised to 80 °C. After stabilizing the temperature, TEOS (2.5 mL, 11.2 mmol) was added drop wise to the surfactant solution and held the reaction mixture for 2 h to give a white precipitate. The solid product was filtered, washed with deionized water and ethanol, dried at 60 °C to yield the as-synthesized MSN. The surface of as-synthesized MSN was functionalized with carboxyl groups to ensure capping by treatment as follows. As-synthesized MSN (300 mg) was refluxed for 12 h in 20 mL anhydrous toluene, containing 300 μL APTES, to functionalize amine group. After centrifugation and washing with ethanol, amine-functionalized MSN was redispersed in 20 mL of DMSO with succinic anhydride (100 mg) and triethylamine (100 μL) and stirred at 50 °C for 24 h to yield the MSN-COOH. To remove the template (CTAB), the MSN-COOH was refluxed for 6 h in acidic methanolic solution.

2.4. Loading, capping and release experiments

Typically, blank MSN-COOH powder (50 mg) was dispersed into 1 mL DMSO, containing 10 mg CPT, and stirred at room temperature for overnight to load hydrophobic drug. The solution was then centrifuged and dispersed in water and further stirred for 6 h, followed by addition of 25 mg EDC·HCl and 200 mg Mn_3O_4 nanocrystals (dispersed in water). The mixture was stirred for another 10 min. The precipitate was centrifuged, it was then dialyzed (molecular weight cut-off = 8 kDa) against distilled water for 2 days to remove the CPT from uncapped nanochannels. All the washings including before capping were collected to calculate the final loading amount. To investigate the redox-responsive properties of $Mn_3O_4@MSN@CPT$ formulation, 5 mg sample was first dispersed in 5 mL of PBS with different concentration of GSH or DTT, then put in a dialysis bags and dialyzed against 45 mL of respective solutions in outside vial. The released quantity of CPT was collected at predetermined time intervals and analyzed by UV/Vis spectroscopy at 365 nm.

2.5. Cell culture and in vitro cell viability assay

Pancreatic cancer cells (BxPC-3) were grown in monolayer in Dulbecco's Modified Eagle's Medium (DMEM, Gibco) supplemented with 5% (v/v) fetal bovine serum (FBS, Gibco) and penicillin/streptomycin (100 U/ml and 100 μg/ml, respectively, Gibco) in a humidified 5% CO_2 atmosphere at 37 °C. Cell viability was investigated by measuring the ability of cells to transform MTT to a purple formazan dye. For MTT assay, BxPC-3 cells were seeded into 96-well plates at a density of $8*10^3$ cells per well in 100 μL of media and grown overnight. The cells were then incubated with various $[Mn^{2+}]$ concentrations of $MnCl_2·4H_2O$, Mn_3O_4, MSN-COOH, $Mn_3O_4@MSN@CPT$ and the corresponding concentrations of free CPT. After incubation for 72 h, 10 μL/well of MTT solution (5 mg/L phosphate buffered saline) was added for another 4 h. The precipitated formazan violet crystals were dissolved in 100 μL of 10 % SDS in 10 mmol HCl solution at 37 °C overnight. The colour intensity of the formazan solution, which reflects the cell growth condition, was measured at 570 nm by multi-detection microplate reader (SynergyTM HT, BioTek Instruments, USA).

2.6. In vitro and in vivo MR Imaging

The T1 MRI in vitro experiments were investigated with a 3.0 T clinical MRI scanner (Siemens Medical Systems) with the following parameters: echo time (TE) = 2.46 ms, repetition time (TR) = 440 ms, slice thickness = 3 (1) mm, flip angle 90 o, field of view (FoV) 260 × 260 mm2. Aqueous dilutions of samples, dispersed in 0.5 % agarose gel, with different [Mn] were placed in tubes. All MR images were then analyzed by using Syngo fastView software. Relaxivity values of r1 were calculated by a series of T1 values, when plotted as 1/T1 according to different [Mn]. The influences of Mn_3O_4 nanocrystals, in culturing cancer cells, on MR signal were also tested. After incubation of a certain amount of Mn_3O_4

nanocrystals for different time, the adherent cells were removed by a mild treatment with trypsin and then transferred into tube for MR test.

In-vivo MRI scans were carried out on mice, using special mouse coil (Siemens). The mice were provided by Norman Bethune College of Medicine (Jilin University). All animal studies were conducted under a protocol approved by the institutes of animal care and use committee. The parameters used for T1 imaging were: echo time (TE) =16 ms, repetition time (TR) =456 ms, slice thickness = 1 mm, flip angle 90 o, field of view (FoV) 143×180 mm^2. During MRI test the mouse were anesthetized by introperotoneal injection (200 μL per 100 g) of chloral hydrate (10 %).

3. Results and discussion

MCM-41-based MSN were synthesized via sol-gel chemistry.[38] The MSN material was then surface-functionalized with carboxylic groups to ensure capping of drug loaded nanochannels (denoted as MSN-COOH). Poorly water-soluble antitumor drug (camptothecin, CPT) was selected as the model drug and loaded into the pores of MSN, and the loading amount was significantly high (53.2 mg/g) compared to those reported in previous studies.[12] Meanwhile, manganese oxide nanolids were prepared using a really facile route. Otherwise, high-temperature methods are routinely used to synthesize hydrophobic nanoparticles in the presence of organic surfactants and solvents.[39, 40] However, hydrophobic nanoparticles thus obtained require tedious and time-consuming ligand exchange approaches to render them water dispersible

In this work, no organic capping ligands were needed in the course of synthesis. After treating Mn_3O_4 with 3-aminopropyltriethoxysilane (APTES), a transparent aqueous solution of amine-functionalized Mn_3O_4 nanolids (Mn_3O_4-NH_2) was obtained. The resulting nanolids were subsequently used to cap CPT loaded MSN-COOH orifices via EDC chemistry, in order to minimize the premature release of a cytotoxic drug. Addition of gate-opening triggers, reducing agents such as GSH or DTT, would then uncap the mesopores by redox assisted dissolution of Mn_3O_4, allowing the release of the drug molecules.

To investigate this capped system, scanning electron microscopy (SEM) and transmission electron microscopy (TEM) techniques were first used to determine the interaction between MSN and Mn_3O_4 nanocrystals. MSN showed smooth surfaces with diameters of ~100 nm in SEM micrograph, whereas 2 nm wide channels were visible in TEM images (Supporting Information Fig. S1a, b). The particle size of Mn_3O_4–NH_2 nanocrystals was found to be in 5-7nm range (Supporting Information Fig. S2). After capping, CPT loaded $Mn_3O_4@MSN$ nanocarriers acquired a scabrous surface compared to original MSN, as evidenced from both SEM and TEM micrographs due to the presence of studded dark spots, which blocked the nanochannels (Fig. 2a, b, c, d).

Small and wide angle X-ray diffraction (XRD) analysis is performed to validate the drug loading and pore capping procedures. The intensity of characteristic MCM-41type peak is markedly reduced in drug loaded and Mn_3O_4 conjugated nanocarrier (Mn_3O_4@MSN@CPT) due to the contrast and
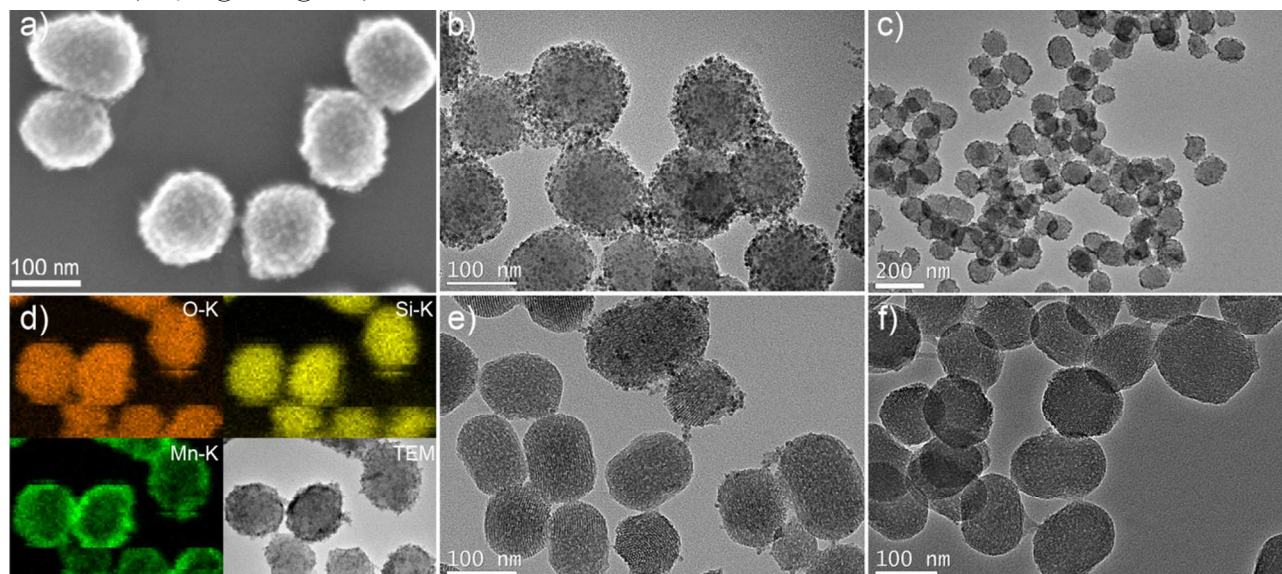

Fig. 2 (a) SEM and (b) (c) TEM micrographs of Mn_3O_4 capped MSN. (d) Images of high-angle annular dark-field scanning TEM and energy-dispersive X-ray elemental mapping of Mn_3O_4@MSN@CPT. (e), (f) TEM micrographs of the sample obtained. after incubation in 0.5 mM and 1.0 mM GSH solutions, showing the dissolution of the Mn_3O_4 nanolid.

disordered product (Fig. 3f). Figure 3e indicates characteristics peaks of Mn_3O_4, the broadness of these peaks can be ascribed to ultrasmall particles size of desired nanolids. Moreover, crystallite size is determined by using Scherer equation. According to XRD data the crystallite size is found to be 7.4 nm. XRD results also validate the conjugation of Mn_3O_4 onto the surface of MSN in terms of reduction in the intensity of characteristics Mn_3O_4 peaks. X-ray photoelectron spectroscopy (XPS) shed some light on Mn_3O_4 and MSN conjugation.

In the survey region (0−1200 eV), carbon, nitrogen, manganese, silicon and nitrogen elements were identified. Since Mn_3O_4 nanoparticles are comprised of manganous and manganic ions, so deconvulation of Mn peak provides two typical peaks at 652.9 and 641.1 eV, which are ascribed to Mn $2p_{1/2}$ and Mn $2p_{3/2}$ spin–orbit states of Mn_3O_4. Energy-dispersive spectroscopy (EDS) also confirms capping of drug loaded nanochannels through Mn_3O_4 nanolids. (Fig. S3). Mn_3O_4–NH_2 nanocrystals were characterized by Infra-red (IR) (Fig. S4).

Since nitrogen adsorption analysis is usually used to evaluate material in terms of surface area and pore volume, therefore, we have carried out nitrogen adsorption−desorption study to determine the effect of drug loading and pore capping on surface area (Fig. S5). The BET surface area is decreased from 893.8 cm^2 g^{-1} to 728.3 cm^2 g^{-1} after CPT loading, whereas the pore volume likewise reduced from 0.761 cc/g to 0.646cc/g respectively. Expectedly, the capping step further lowered the surface area and pore volume to 209.3 cm^2g^{-1}, 0.42 cc/g respectively.

This study is particularly interesting in term of reduction-induced dissolution of paramagnetic nanolids from the surface of drug loaded mesopores. GSH is a common reducing agent within cells. However, compared to those in normal tissue, GSH levels in human cancer tissues such as breast,[41-43] colon,[44] and lung[45, 46] are demonstrated to be fairly high. Both DTT and GSH, commonly used reducing agent, were used in this study as an external stimulus model for the reducing environment of the cytoplasm. Since Mn_3O_4 is comprised of both Mn(II) and Mn(III) species, it was envisaged that the high intracellular reducing environment in tumor cells reduced Mn(III) into manganese (II), thus disintegrating the Mn_3O_4 solid nanoparticles into water soluble Mn (II) ions.
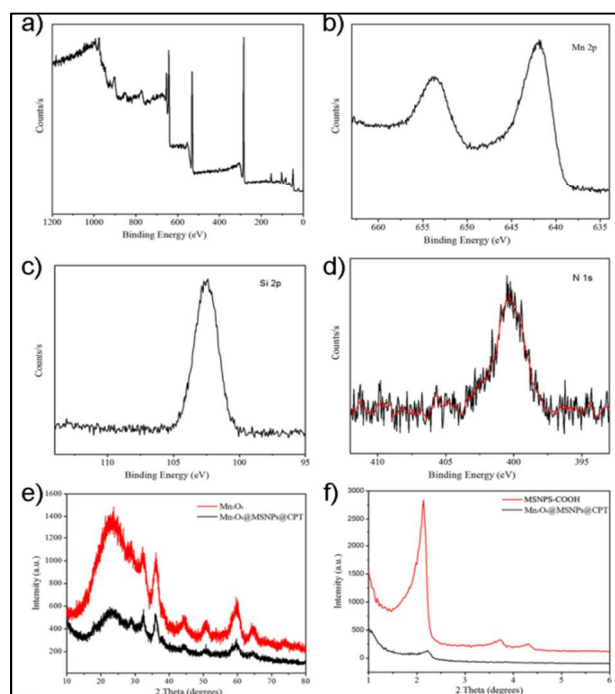
**Fig. 3** (a), (b), (c), (d) XPS spectrum of Mn_3O_4@MSN nanocomposite. (a) Full survey spectrum, (b) Mn 2p peak, (c) Si 2p peak, (d) N 1s peak. (e) Wide-angle Mn_3O_4@MSN and Mn_3O_4 nanocrystal peaks. (f) Low-angle X-ray diffraction (XRD) patterns of Mn_3O_4@MSN and MSN-COOH peaks.

As a proof-of-concept study to validate reduction induced dissolution of paramagnetic "gatekeeper", we dispersed Mn_3O_4@MSN@CPT or Mn_3O_4 nanocrystals in phosphate-buffered saline (PBS) solution containing DTT and GSH at various concentrations (Fig. 4a, b). Notably, these in vitro experiments furnishes an opprotunity to gain some insight about the dissolution control drug release mechanism, moreover, we can predict a similar in vivo drug release behavior after redox mediated dissoluion of magnetic nanolids. In the absence of any reducing agents, a flat baseline was obtained, and less than 6 % CPT was leached from drug formulation. In contrast, with the introduction of DTT or GSH of different amounts, CPT release profile displayed an obvious increasing trend, suggesting the dissolution of Mn_3O_4 to unleash the loaded drug molecules. The dissolution process of Mn_3O_4 was also verified by the gradual disappearance of the dark dots from MSN surface as revealed in TEM images (Fig. 2e, f and Supporting Information Fig. S1a,b).

Incubation of capped sample in the presence of reducing agents of different kinds and concentrations led to a more revealing and convincing proof of Mn_3O_4 disintegration. Significant fading of dark brown colour of Mn_3O_4 was observed along with

increasing time and concentration of GSH (Fig. 4c). To further evaluate our hypothesis of redox-induced dissolution, inductively coupled plasma (ICP) analysis was carried out to detect the concentration of manganese ions after subjecting Mn_3O_4 to different concentration of GSH (Fig. 4d). It was found that there was no manganese ions leached out within 12 h in the absence of GSH treatment. However, treatment of Mn_3O_4 nanocrystals with GSH resulted in increasing concentration of manganese ions, which lend strong support to our proposed ideas that manganese ions leached from Mn_3O_4 into liquid phase gradually.
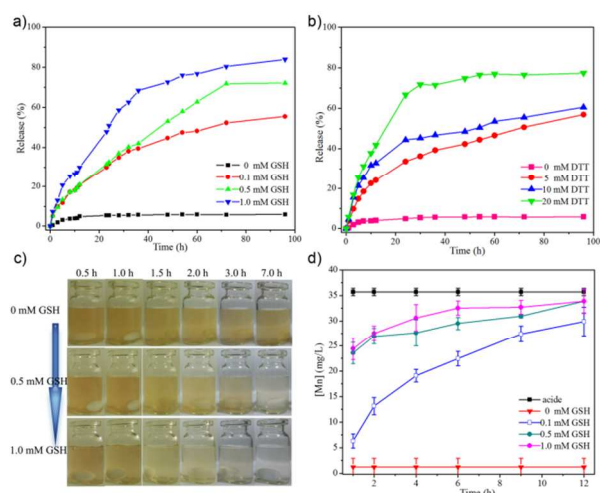
Fig. 4 (a) Release profiles of Mn_3O_4@MSN@CPT formulation in 0, 0.1, 0.5, 1.0 mM of GSH. (b) Release profiles of Mn_3O_4@MSN@CPT in 0, 5, 10, 20 mM of DTT. (c) Photographs of Mn_3O_4@MSN incubated in different concentration of GSH, confirming the dissolution of paramagnetic nanocrystals (d) inductively coupled plasma (ICP) analysis after subjecting Mn_3O_4 nanocrystals to different concentration of GSH.

Raman spectra of GSH, oxidized glutathione (GSSG) and the final product of Mn_3O_4 dissolution in GSH solution respectively were shown in Fig. 5. A characteristic band at 2579 cm^{-1} (S-H stretching) was observed in mere glutathione sample; however, after the addition of Mn_3O_4 solution the thiol (S-H) peak was disappeared and subsequently a new band at 511 cm^{-1} (S-S stretching) was appeared, demonstrating the dimerization of glutathione. More importantly, the typical Mn_3O_4 peak (~650 cm^{-1}) is absent after the exposure of GSH, thus establishing the dissolution of Mn_3O_4. Two prominent peaks at 3404 cm^{-1} and 3422 cm^{-1} are ascribed N-H stretching, derived from amine moiety of APTES. This result indicates the GSH molecules are oxidized after reacting with Mn_3O_4. It also sheds some light on mechanism and suggests that Mn_3O_4 dissolution was carried out via thiol-disulfide transformation, and resultantly GSSG is produced as shown in the equation (Figure 5).[47]

Nanoscale Accepted Manuscript
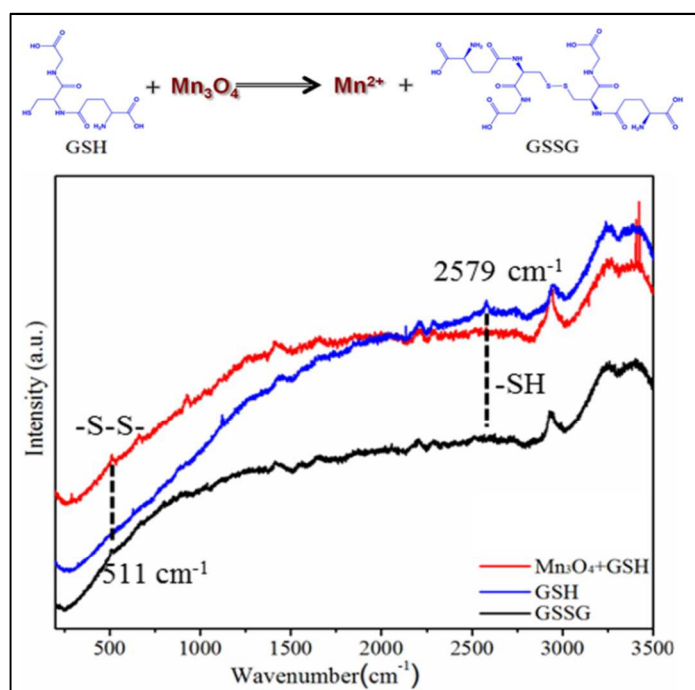
Fig. 5 Schematic diagram shows the dimerization of glutathione after reacting with Mn_3O_4 nanopartices and the Raman spectra of GSH, GSSG and GSH after treatment with Mn_3O_4 nanocrystals.

In order to assess the biological properties of our capping system, MTT assay was performed by using pancreatic cancer cells (BxPC-3) (Fig. 6a, b, c). The cytotoxicity of Mn^{2+} ions (as $MnCl_2$), Mn_3O_4 nanocrystals, capping sample and free CPT was estimated. Firstly, the cytotoxicity of Mn_3O_4 nanocrystals, manganese ion and Mn_3O_4@MSN were compared, which showed that all species displayed a similar cell viability performance at low concentration. However, at high equivalent concentration, Mn_3O_4 nanocrystals exhibited fairly low cytotoxicity compared with Mn^{2+}. Mn_3O_4@MSN shows the same behavior with Mn_3O_4 nanocrystals. Based on these results, we supposed that the relatively high levels of intracellular reducing agents lead to slow disintegration of Mn_3O_4 to yield cytotoxic Mn^{2+} ions, as was proved by the high killing

Journal Name

ARTICLE
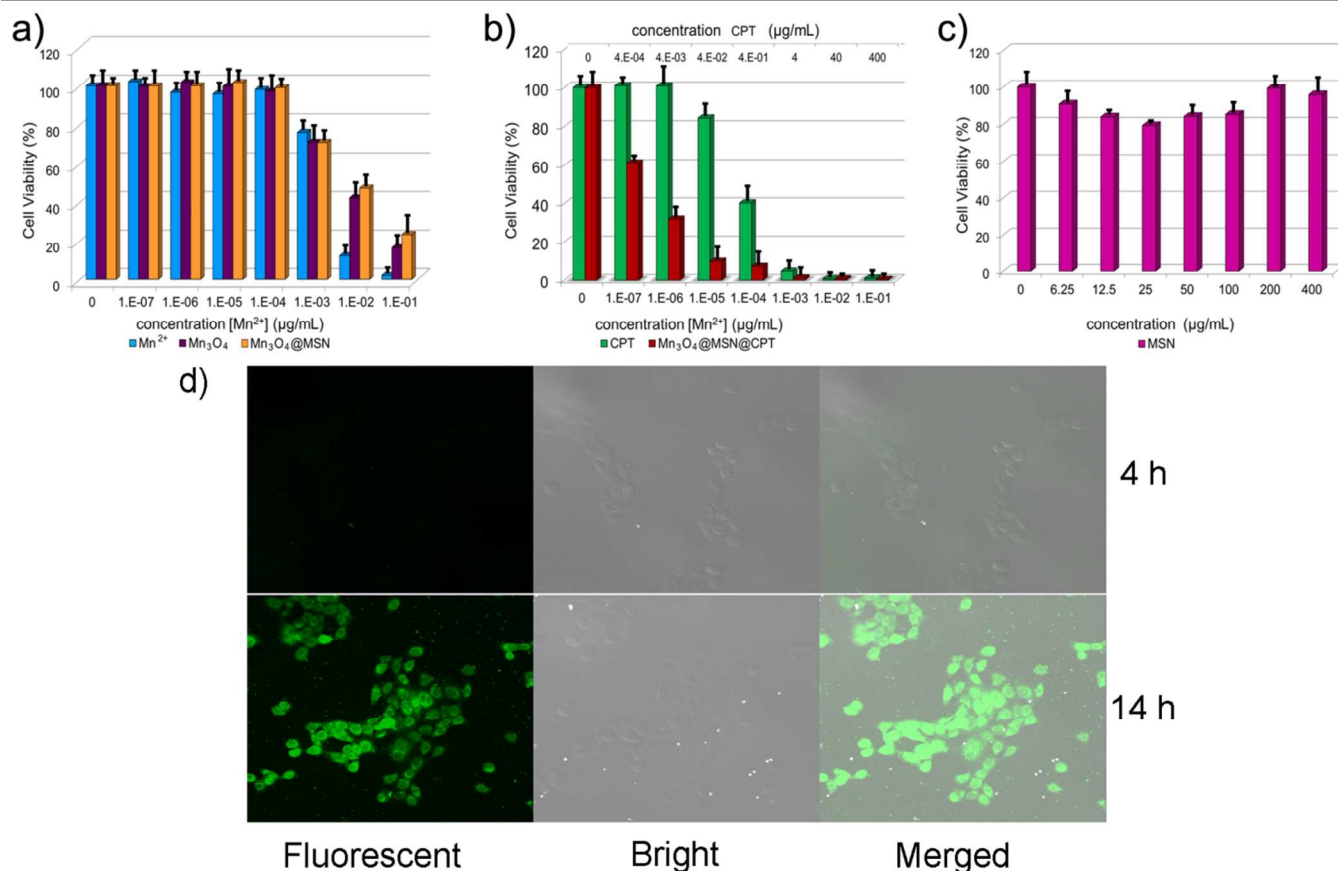
Fig. 6 (a) In vitro viability of BxPC-3 cells in the presence of Mn^{2+}, Mn_3O_4 nanolids and Mn_3O_4@MSN, (b) Mn_3O_4@MSN@CPT, free CPT, And (c) MSN functionalized with carboxyl groups, incubation time was 72 h. Values are the average of three separate experiments in triplicate and are expressed as mean $+\square$SD. *p $<\square$0.05. (d) Fluorescence confocal images of "Mn_3O_4@MSN@rhodamine 6G" nanoparticles and their uptake by BxPC-3 cancer cells in different time. No obvious fluorescence was observed within the cells that were incubated with 4 h

efficiency of manganese ions compared to Mn_3O_4 nanocrystals at low concentrations.

Therefore, we can infer that Mn_3O_4 nanocrystal itself exhibits no cytotoxicity until transformed into manganese ion. Expectedly, drug loaded Mn_3O_4@MSN exhibited much higher cytotoxic effect on pancreatic cancer cells growth and proliferation than that observed with equivalent dose of free CPT in the culture medium. When the drug formulation displayed potent cytotoxic activity at the therapeutic concentration, the Mn_3O_4 nanolids exhibited no cytotoxic potential, which proved the biocompatibility of Mn_3O_4 nanocrystals. The improvement of the cell inhibitory performance of hydrophobic CPT should be credited to hydrophilic mesoporous nanocarriers which not only ensured the controlled release of water insoluble CPT, but also realized a highly needed site specific targeted drug release.

To visualize in vitro dissolution and encapsulated cargo release, confocal microscopy was checked by loading rhodamine 6G as a model dye. Fig. 6d shown the confocal images of BxPC-3 cells treated with differentnt rhodamine 6G loaded Mn_3O_4@MSN nanoformulations in different times (4 h and 12 h), whereas working parameters remains constant in every experiment. Four hours incubation resulted in a negligible staining of cancer cells, however, after 12 h incubation a significant increase in the fluorescence of Rhodamine 6G was observed. Initially, most of the nanolids were intact and rhodamine 6G molecules were still confined inside the MSN within 4 h, but prolonged incubation time permits responsive and sustained release of the cargo into cell. Taken together, cell micrographs varifies the slow dissolution of the Mn_3O_4 nanocrystals and subsequent sustained release of drug over the period of time.

As Mn_3O_4 exhibits T1 effects, utilization of drug loaded paramagnetic nanocrystals capped MSN as T1 MRI contrast agent is indeed a judicious choice to be executed. To evaluate the effectiveness of Mn_3O_4@MSN@CPT as MRI contrast agents, in vitro experiments were performed. Fig. 7a, b, c showed the capping sample when subjected to T1 MRI. As the concentration of manganese was increased, enhancement in the magnetic resonance signal was observed, thus establishing its potential application as a T1 contrast agent. The relaxivity value (r1) of the NPs was found to be 13.39 $mM^{-1}s^{-1}$. It was interesting to note that after the disintegration of the capping agent (Mn_3O_4 nanolids) by GSH, the signals of magnetic resonance were greatly improved and r1 value was almost 2 times increased to 25.17 $mM^{-1}s^{-1}$. This phenomenon can be explained by redox-mediated leaching of manganese ions from Mn_3O_4. The resulting free manganese ions can readily interact with nearby water molecules to enhance T1 signal. To decide the biological applicability of this system, in vitro cell study was also performed (Fig. 7d). The incubation of Mn_3O_4 nanocrystals with BxPC-3 cells led to a pronounced increase in T1 signal with increasing incubation time. In vitro cell study also suggested that cancer cells are capable of dissolving Mn_3O_4 nanocrystals at a steady rate, because of high intracellular GSH concentration. Moreover, we extended the system to in vivo environment, and carried out MR test by in vivo injection of nanoformulation (2 mg of Mn per kg of mouse body weight). As a result, series of T1 images were obtained as shown in Fig. 7e. In comparison with pre-contrast images, an obvious signal enhancement both in kidney and liver was noticed with increasing time, indicating the potential utility of our strategy.
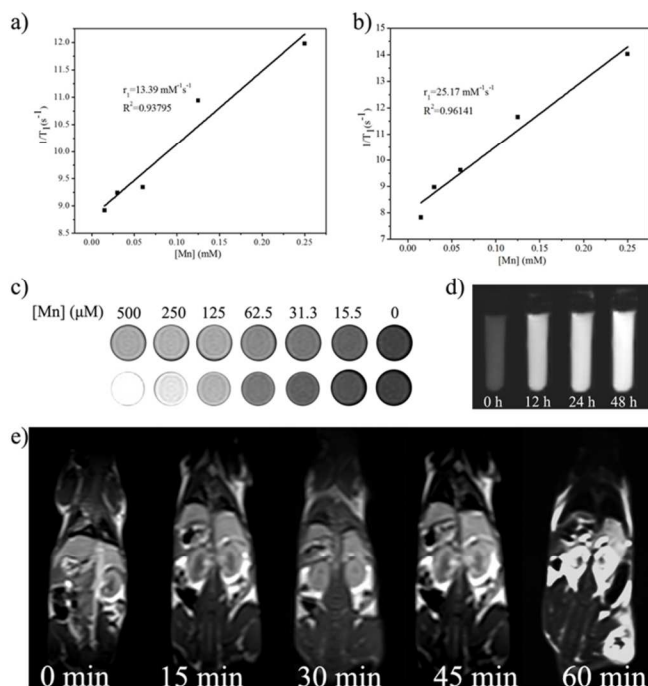
panel) and after (down panel) the dissolution of Mn_3O_4 T1 weighted MR images of dispersed Mn_3O_4@MSN at different Mn concentrations in 0.5 % agarose. (d) In vitro cell study of Mn_3O_4@MSN incubated in BxPC-3 cells with different incubation time (with Mn concentration 0.1 μg/mL). (e) A series of 3.0 T in vivo T1 MRI of a mouse with time after injection of a Mn_3O_4@MSN solution into a mouse tail vein.

4. Conclusions

In conclusion, we have developed a sophisticated nanotheranostic system, using Mn_3O_4 nanoparticles to cap drug loaded channels of mesoporous silica for simultaneously performing intelligent drug delivery and redox-activated contrast-enhanced MRI. Manganese oxide nanoparticles are demonstrated to be highly susceptible to intracellular redox environment, and readily undergo dissolution when exposed to highly prevalent intracellular reducing agent glutathione. As a result, channels of silica are opened to release loaded drug molecules, leading to target specific therapeutic response against cancer cells. Most prominently, redox assisted dissolution of Mn_3O_4 nanolids to manganese ions also led to twofold increase in T1 signal. We envision that our results would prove a significant step in personalized medicine and provide a synergistic strategy to enhance therapeutic and imaging efficiency.

Acknowledgements

Notes and references

[a] State Key Laboratory of Inorganic Synthesis and Preparative Chemistry, College of Chemistry, Jilin University, Changchun, 130012, China, Fax: (+86) 431-516-8331, Tel: (+86) 431-516-8331, E-mail: zhugs@jlu.edu.cn
[b] Queensland Micro- and Nanotechnology Centre, Griffith University, Nathan QLD 4111, Australia.
[c] Radiology Department, The First Hospital of Jilin University, Changchun,130021, China
[d] College of Life Science, Jilin University, Changchun,130012, China
[e] College of Construction Engineering, Jilin University, Changchun,130026
Corresponding author: Email address: zhugs@jlu.edu.cn

Fig. 7 (a) Before and (b) after the dissolution of Mn_3O_4 nanocrystals, T1 relaxation rate plots rate (1/T1) of versus of Mn Concentration. (c) Before (top

1.   M. E. Davis, Z. Chen and D. M. Shin, *Nat. Rev. Drug Discov.*, 2008, **7**, 771-782.
2.   L. Zhang, F. X. Gu, J. M. Chan, A. Z. Wang, R. S. Langer and O. C. Farokhzad, *Clin. Pharmacol. Ther.*, 2007, **83**, 761-769.
3.   V. R. Devadasu, V. Bhardwaj and M. N. V. R. Kumar, *Chem. Rev.*, 2012, **113**, 1686-1735.
4.   D. Peer, J. M. Karp, S. Hong, O. C. Farokhzad, R. Margalit and R. Langer, *Nat. Nano.*, 2007, **2**, 751-760.
5.   M. Arruebo, R. Fernández-Pacheco, M. R. Ibarra and J. Santamaría, *Nano Today*, 2007, **2**, 22-32.

6. I. Meerovich, A. Koshkaryev, R. Thekkedath and V. P. Torchilin, *Bioconjugate Chem.*, 2011, **22**, 2271-2282.
7. Q. Huo, J. Liu, L.-Q. Wang, Y. Jiang, T. N. Lambert and E. Fang, *J. Am. Chem. Soc.*, 2006, **128**, 6447-6453.
8. L. M. Kaminskas, V. M. McLeod, B. D. Kelly, C. Cullinane, G. Sberna, M. Williamson, B. J. Boyd, D. J. Owen and C. J. H. Porter, *Mol. Pharm.*, 2012, **9**, 422-432.
9. W. Wu, S. Wieckowski, G. Pastorin, M. Benincasa, C. Klumpp, J.-P. Briand, R. Gennaro, M. Prato and A. Bianco, *Angew. Chem. Int. Ed.*, 2005, **44**, 6358-6362.
10. N. Chanda, V. Kattumuri, R. Shukla, A. Zambre, K. Katti, A. Upendran, R. R. Kulkarni, P. Kan, G. M. Fent, S. W. Casteel, C. J. Smith, E. Boote, J. D. Robertson, C. Cutler, J. R. Lever, K. V. Katti and R. Kannan, *PNAS*, 2010, **107**, 8760-8765.
11. M. Liong, J. Lu, M. Kovochich, T. Xia, S. G. Ruehm, A. E. Nel, F. Tamanoi and J. I. Zink, *ACS NANO*, 2008, **2**, 889-896.
12. J. Lu, M. Liong, J. I. Zink and F. Tamanoi, *Small*, 2007, **3**, 1341-1346.
13. I. I. Slowing, J. L. Vivero-Escoto, C.-W. Wu and V. S. Y. Lin, *Adv. Drug Deliv. Rev.*, 2008, **60**, 1278-1288.
14. V. Cauda, C. Argyo, A. Schlossbauer and T. Bein, *J. Mater. Chem.*, 2010, **20**, 4305-4311.
15. R. Liu, Y. Zhang, X. Zhao, A. Agarwal, L. J. Mueller and P. Y. Feng, *J. Am. Chem. Soc.*, 2010, **132**, 1500-1501.
16. H. P. Rim, K. H. Min, H. J. Lee, S. Y. Jeong and S. C. Lee, *Angew. Chem. Int. Ed.*, 2011, **50**, 8853-8857.
17. C. Y. Lai, B. G. Trewyn, D. M. Jeftinija, K. Jeftinija, S. Xu, S. Jeftinija and V. S. Y. Lin, *J. Am. Chem. Soc.*, 2003, **125**, 4451-4459.
18. X. Ma, K. T. Nguyen, P. Borah, C. Y. Ang and Y. L. Zhao, *Adv. Healthcare Mater.*, 2012, **1**, 690-697.
19. N. Mas, A. Agostini, L. Mondragon, A. Bernardos, F. Sancenon, M. D. Marcos, R. Martinez-Manez, A. M. Costero, S. Gil, M. Merino-Sanjuan, P. Amoros, M. Orzaez and E. Perez-Paya, *Chem. Eur. J.*, 2013, **19**, 1346-1356.
20. J. Zhang, Z.-F. Yuan, Y. Wang, W.-H. Chen, G.-F. Luo, S.-X. Cheng, R.-X. Zhuo and X.-Z. Zhang, *J. Am. Chem. Soc.*, 2013, **135**, 5068-5073.
21. D. P. Ferris, Y.-L. Zhao, N. M. Khashab, H. A. Khatib, J. F. Stoddart and J. I. Zink, *J. Am. Chem. Soc.*, 2009, **131**, 1686-1688.
22. Q. Yuan, Y. Zhang, T. Chen, D. Lu, Z. Zhao, X. Zhang, Z. Li, C.-H. Yan and W. Tan, *ACS NANO*, 2012, **6**, 6337-6344.
23. A. Schlossbauer, J. Kecht and T. Bein, *Angew. Chem. Int. Ed.*, 2009, **48**, 3092-3095.
24. C. R. Thomas, D. P. Ferris, J.-H. Lee, E. Choi, M. H. Cho, E. S. Kim, J. F. Stoddart, J.-S. Shin, J. Cheon and J. I. Zink, *J. Am. Chem. Soc.*, 2010, **132**, 10623-10625.
25. Y. Zhu, H. Liu, F. Li, Q. Ruan, H. Wang, M. Fujiwara, L. Wang and G. Q. Lu, *J. Am. Chem. Soc.*, 2010, **132**, 1450-1451.
26. F. Muharnmad, M. Y. Guo, W. X. Qi, F. X. Sun, A. F. Wang, Y. J. Guo and G. S. Zhu, *J. Am. Chem. Soc.*, 2011, **133**, 8778-8781.
27. G. Zhang, Y. Liu, Q. Yuan, C. Zong, J. Liu and L. Lu, *Nanoscale*, 2011, **3**, 4365-4371.
28. W. Zhang, X.-W. He, Y.-Q. Yang, W.-Y. Li and Y.-K. Zhang, *J. Mater. Chem. B*, 2013, **1**, 347-352.
29. K. Ma, H. Sai and U. Wiesner, *J. Am. Chem. Soc.*, 2012, **134**, 13180-13183.
30. H. Yang, Y. Zhuang, H. Hu, X. Du, C. Zhang, X. Shi, H. Wu and S. Yang, *Adv. Funct. Mater.*, 2010, **20**, 1733-1741.
31. J. J. Davis, W.-Y. Huang and G.-L. Davies, *J. Mater. Chem.*, 2012, **22**, 22848-22850.
32. B. Chang, J. Guo, C. Liu, J. Qian and W. Yang, *J. Mater. Chem.*, 2010, **20**, 9941-9947.
33. J. E. Lee, N. Lee, H. Kim, J. Kim, S. H. Choi, J. H. Kim, T. Kim, I. C. Song, S. P. Park, W. K. Moon and T. Hyeon, *J. Am. Chem. Soc.*, 2010, **132**, 552-557.
34. J. Kim, H. S. Kim, N. Lee, T. Kim, H. Kim, T. Yu, I. C. Song, W. K. Moon and T. Hyeon, *Angew. Chem. Int. Ed.*, 2008, **47**, 8438-8441.
35. T. Kim, E. Momin, J. Choi, K. Yuan, H. Zaidi, J. Kim, M. Park, N. Lee, M. T. McMahon, A. Quinones-Hinojosa, J. W. M. Bulte, T. Hyeon and A. A. Gilad, *J. Am. Chem. Soc.*, 2011, **133**, 2955-2961.
36. H. Hu, A. Dai, J. Sun, X. Li, F. Gao, L. Wu, Y. Fang, H. Yang, L. An, H. Wu and S. Yang, *Nanoscale*, 2013, **5**, 10447-10454.
37. F. Hu and Y. S. Zhao, *Nanoscale*, 2012, **4**, 6235-6243.
38. C.-Y. Lai, B. G. Trewyn, D. M. Jeftinija, K. Jeftinija, S. Xu, S. Jeftinija and V. S. Y. Lin, *J. Am. Chem. Soc.*, 2003, **125**, 4451-4459.
39. T. Kim, E.-J. Cho, Y. Chae, M. Kim, A. Oh, J. Jin, E.-S. Lee, H. Baik, S. Haam, J.-S. Suh, Y.-M. Huh and K. Lee, *Angew. Chem. Int. Ed.*, 2011, **50**, 10589-10593.
40. H. B. Na, J. H. Lee, K. An, Y. I. Park, M. Park, I. S. Lee, D.-H. Nam, S. T. Kim, S.-H. Kim, S.-W. Kim, K.-H. Lim, K.-S. Kim, S.-O. Kim and T. Hyeon, *Angew. Chem.*, 2007, **119**, 5493-5497.
41. M. Raderer and W. Scheithauer, *Cancer*, 1993, **72**, 3553-3563.
42. R. R. Perry, J. Mazetta, M. Levin and S. C. Barranco, *Cancer*, 1993, **72**, 783-787.
43. K. Lee, H. Lee, K. H. Bae and T. G. Park, *Biomaterials*, 2010, **31**, 6530-6536.
44. S. M. S. Redmond, F. Joncourt, K. Buser, A. Ziemiecki, H.-J. Altermatt, M. Fey, G. Margison and T. Cerny, *Cancer Research*, 1991, **51**, 2092-2097.
45. J. A. Cook, H. I. Pass, S. N. Iype, N. Friedman, W. DeGraff, A. Russo and J. B. Mitchell, *Cancer Research*, 1991, **51**, 4287-4294.
46. T. Schnelldorfer, S. Gansauge, F. Gansauge, S. Schlosser, H. G. Beger and A. K. Nussler, *Cancer*, 2000, **89**, 1440-1447.
47. S. Kumar, W.-K. Rhim, D.-K. Lim and J.-M. Nam, *ACS NANO*, 2013, **7**, 2221-2230.

Nanoscale Accepted Manuscript

Table of Contents
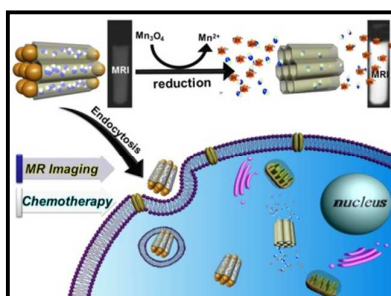
Redox sensitive dissolution of paramagnetic NPs (Mn_3O_4) results in a controlled drug release and enhanced magnetic resonance imaging.